Influence of microstructure on work-hardening and ductile fracture of aluminium alloys

Ketill O. Pedersen[a,b] , Ida Westermann[a,b], Trond Furu[c], Tore Børvik[a,*] and Odd Sture Hopperstad[a]

[a] *Structural Impact Laboratory (SIMLab), Centre for Research-based Innovation, Department of Structural Engineering, Norwegian University of Science and Technology, NO-7491 Trondheim, Norway*

[b] *SINTEF Materials & Chemistry, NO-7465 Trondheim, Norway*

[c] *Norsk Hydro, Corporate Technology Office, NO-0283 Oslo, Norway*

Abstract

The effect of microstructure on the work-hardening and ductile fracture of aluminium alloys was studied using an experimental-numerical approach. Four aluminium alloys with different strength and particle content were tested in uniaxial tension after the following subsequent processing steps: 1) casting and homogenization, 2) extrusion, and 3) cold rolling followed by heat treatment. The latter processing step was carried out to obtain a recrystallized grain structure with random crystallographic texture. The alloys were two AlFe alloys with different Fe content, one AlMn alloy and one AlMgSi alloy. The grain structure, particle distribution and crystallographic texture were determined for all combinations of alloy and processing route using optical and scanning electron microscopy. Tensile tests were carried out on axisymmetric samples to obtain the true stress-strain curves to failure and the true failure strain of the materials, using a laser-based measuring system. Based on numerical simulations of the tensile tests, the equivalent stress-strain curves were determined to failure, assuming J_2 flow theory. The results showed that the microstructure had a marked effect on both work-hardening and ductility, while the ductile fracture mechanism remained unchanged. The plastic anisotropy, induced by the extrusion process and not entirely removed by the cold rolling and heat treatment, led to a wide range of fracture modes of the axisymmetric samples. The failure strain was markedly lower for the cast and homogenized material than for the extruded and the cold rolled and recrystallized materials of the same alloy. The failure strain was further found to decrease linearly with the yield stress for similar microstructure.

Keywords: Aluminium alloys; experimental-numerical method; plastic behaviour; fracture behaviour; scanning electron microscopy; fractography

[*] Corresponding author. Tel.: + 47-73-59-46-47; fax: + 47-73-59-47-01.

E-mail address: tore.borvik@ntnu.no (T. Børvik).

1. Introduction

The work-hardening of aluminium alloys is important for the formability of aluminium sheets and profiles and the plastic collapse of aluminium structures [1]. A good description of the work-hardening is further important for the modelling of fracture in aluminium structures, since plastic instability in the form of necking is often a precursor to ductile fracture.

Solute elements, hardening precipitates and dispersoids contribute to the yield strength of aluminium alloys, since they act as distributed pinning points for mobile dislocations, thus increasing the shear stress required to move the dislocations. Solute elements also contribute to an increased work-hardening by reducing the dynamic recovery rate. The work-hardening is further increased by non-shearable hardening precipitates and dispersoids that act as sources for generating geometrically necessary dislocations—the result being a strong work-hardening for small strains. Cheng et al. [2] studied the effect of the precipitation state on the yield stress and work-hardening of two age-hardening aluminium alloys, and developed a semi-empirical model to interpret the experimental results, including contributions to the flow stress from solid solution, precipitation and dislocation hardening. Embury et al. [3] discussed the influence of solute elements, precipitate phases, dispersoids and inclusions, and large strains on the work-hardening of aluminium alloys. A combined precipitation, yield strength and work-hardening model for AlMgSi alloys was developed by Myhr et al. [4], where the influence of solute elements and shearable and non-shearable precipitates on the yield strength and work-hardening was incorporated. Recently, the effect of dispersoids on the work-hardening of aluminium alloys was investigated experimentally by Zhao et al. [5]. The study showed that a fine dispersion of non-shearable particles increased the initial work-hardening and reduced the work-hardening at larger plastic strains. This observation was attributed to the generation of geometrically necessary dislocations, and a work-hardening model for aluminium alloys containing dispersoids was proposed.

The ductility of aluminium alloys is influenced significantly by the volume fraction and distribution of intermetallic constituent particles, and in age-hardening alloys also by the precipitate free zones. The constituent particles are large and few compared with the hardening precipitates, i.e., the inter-particle spacing is large, and thus their contribution to the work-hardening becomes limited. Dumont et al. [6] studied the relationship between the microstructure and the strength and toughness of an AA7050 aluminium alloy. The microstructure was varied by changing the quench rate and the ageing time, and the role of the constituent particles, the grain structure and the precipitation state was considered.

Morgeneyer et al. [7] investigated void growth and coalescence in an AA2139 aluminium alloy sheet using high-resolution tomography. It was found that as-received and undeformed material exhibited a distribution of elongated voids aligned in the rolling direction, which resulted in toughness anisotropy. A micromechanics-based damage model was used by Steglich et al. [8] to investigate the anisotropic fracture of the 2024-T351 aluminium alloy, taking into consideration the effect of the void aspect ratio and the void distribution. Jordon et al. [9] studied the influence of primary and secondary void nucleation and growth on the ductility of an AA7075 aluminium alloy and used an internal state variable plasticity/damage model to describe the damage-induced anisotropic material response. In the experimental work by Chen et al. [10], dynamic fracture of AA6xxx and AA7xxx aluminium alloys was studied. Partly transgranular and partly intergranular fracture modes were found for all the investigated alloys. The transgranular fracture was promoted by nucleation of voids at primary particles, and possibly dispersoids for the fibrous alloys, while the precipitation-free zones along the grain boundaries led to intergranular fracture. Pedersen et al. [11] found similar fracture behaviour in an AA7075-T651 alloys under quasi-static, dynamic and impact loading conditions.

In the present work, an experimental-numerical method was used to determine the large-strain work-hardening and ductile failure strain of four aluminium alloys based on tensile tests on axisymmetric specimens. Using a laser-based measuring system in combination with finite element simulations of the tensile tests, the work-hardening curve of the material could be determined to failure. In a previous study by the authors, this method was used to investigate the work-hardening and ductile fracture of the same alloys in the cast and homogenized condition [12]. The materials investigated were two AlFe alloys, one AlMn alloy and one AlMgSi alloy. In the present study, the method was used to study the influence of microstructure on the work-hardening and ductile fracture of these alloys by subjecting them to different thermo-mechanical processes. Through these processing steps, namely casting and homogenization, extrusion, and cold rolling and heat treatment, different microstructures were obtained in terms of grain structure, particle distribution and crystallographic texture. The microstructure of the materials and the fracture surfaces were characterized by optical and scanning electron microscopy, while the particle and solute element contents were estimated using the Alstruc code [13]–[15]. The work-hardening of the material was analysed using the extended Voce rule, where two hardening terms were used to capture the various stages of work-hardening. Similar methods have been applied to analyze work-hardening of several

commercial aluminium alloys in [1], of AA6111 and AA7030 in [2], of single- and multi-phased aluminium alloys in [3], of AA7108 in [16], and of AA7010 in [17].

2. Materials

The four aluminium alloys studied were provided as DC-cast extrusion ingots of 100 mm diameter produced at the laboratory casting facilities at Hydro Aluminium R&D Sunndal. The chemical compositions of the four alloys, henceforth called Al0.2Fe, Al0.8Fe, Al1.2Mn and AlMgSi, are given in Table 1. TiB was added to all alloys as grain refiner to control the grain size and avoid abnormal grains during casting. In this study, these alloys were mainly selected to investigate the effect of microstructure on the work-hardening and ductile fracture behaviour. However, the Al0.2Fe and Al0.8Fe alloys belong to the AA1xxx series, commonly used for food protection and packaging, the Al1.2Mn alloy belongs to the AA3xxx series, used e.g. in air condition condensers and beverage cans, and the AlMgSi alloy belongs to the AA6xxx series, typically used in the building industry, i.e., window frames and wall panels.

Figure 1 shows the different processing steps after casting to which the materials were subjected. The homogenization procedures applied to the ingots are compiled in Table 2, and were carried out in a laboratory furnace. The temperature-time cycles are similar to industrial practice and consist of a soaking treatment followed by a predetermined cooling rate. The ingots were further extruded in an 800 tons laboratory press to rectangular profiles with dimensions 10×50 mm^2 and 20×25 mm^2 using industrial extrusion parameters, i.e., billet temperature of 475°C, container temperature of 435°C and ram speed of 5 mm/s. The extrusion reduction ratio was 16 in both cases and the profiles were cooled in air. The profile with dimensions 10×50 mm^2 was used for making tensile test specimens. Three specimens with tensile axis in the extrusion direction were machined across the width of the profile for each material. The final processing route was obtained by cold rolling the extruded profile from 20×25 mm^2 to 12×12 mm^2 prior to heat treatment at 500°C for 5 minutes and water quenching to achieve a recrystallized grain structure with a texture close to random. The low temperature was used to prevent abnormal grain growth, but it is still above the solvus line for AlMgSi. A similar method was used in [18]. The AlMgSi profile was given a solid solution heat treatment (SSHT) at 540°C for 30 min followed by water quenching before cold rolling.

After each processing step, the materials were tested after storing them at room temperature for more than one week. The materials obtained after the three processing routes are indicated in Figure 1 and were named: 1) cast and homogenized (CH), 2) extruded (EX) and 3) rolled and recrystallized (RR) — and these abbreviations will be used henceforth.

3. Experimental-numerical procedures

3.1 Mechanical testing

Triplicate tensile tests were performed on axisymmetric samples respectively oriented along the longitudinal axis of the cast ingot, the extrusion direction (ED) and the rolling direction (RD) for the four materials. The samples had 6 mm diameter and 40 mm parallel length. The average strain rate in the tests was $5{\cdot}10^{-4}\,\mathrm{s}^{-1}$ before necking. The applied force and the diameter at the minimum cross section of the specimen were measured continuously until fracture, using an in-house measuring rig with two perpendicular lasers that accurately measured the specimen diameter (see [12] for details). The Cauchy (true) stress and the logarithmic (true) strain were calculated as

$$\sigma_t = \frac{F}{A} \quad \text{and} \quad \varepsilon_l = \ln\frac{A_0}{A} \tag{1}$$

where F is the applied force, $A_0 = \frac{\pi}{4} D_0^2$ is the initial cross-section area, and D_0 is the initial diameter of the gauge section. The current area of the cross section was estimated, assuming ellipsoidal geometry, as

$$A = \frac{\pi}{4} D_1 D_2 \tag{2}$$

where D_1 and D_2 are the diameters measured continuously by the laser-based measuring system. Assuming orthotropic symmetry of the EX and RR materials, D_1 and D_2 were measured along the transverse principal axes of anisotropy. The CH materials were assumed to be isotropic. The failure strain was defined as $\varepsilon_f = \ln(A_0 / A_f)$, where A_f is the cross-section area at failure—here assumed to occur at the maximum value of the Cauchy stress.

3.2 Microstructure characterization

Samples of all the 12 materials (four alloys and three processing routes) were mechanically ground and polished followed by electro polishing. The distribution of the particles was obtained by image processing of back-scattered electron (BSE) micrographs taken in a Hitachi SU-6600 FESEM operated at 5 kV. To reveal the grain structure in the optical microscope, polished specimens were also anodized at room temperature for 2 min using $\mathrm{HBF_4}$. Fracture surfaces of the failed tensile tests were investigated in a Zeiss Gemini Supra 55 VP FESEM operated at 10 kV.

The texture of the 12 materials was determined using the electron back-scatter diffraction (EBSD) technique in the Hitachi SU-6600 FESEM operated at 20 kV. The EBSD measurements were carried out in a random plane for the CH materials, in the ED/ND plane for the EX materials, and in the RD/ND (or RD/TD) plane for the RR materials, where ND is the normal direction and TD is the transverse direction of the profile. A step size of 5 μm was used, and a minimum of 800 and up to 2000 grains were investigated. The data was rotated into the standard coordinate system ((RD, TD, ND) = (*X*, *Y*, *Z*)) before the orientation distribution functions (ODF) were calculated by the EDAX TSL OIM software. A harmonic series expansion and average grain orientation weighted by the grain size were used in the calculations. Triclinic sample symmetry was used for the CH and RR materials, whereas orthotropic sample symmetry was used for the EX materials.

To examine the microstructure evolution and the fracture mechanisms, the failed tensile specimens were sliced and the cross section in the longitudinal direction was polished and investigated for the various materials in the scanning electron microscope.

In [12], the volume fractions of particles and solute elements in the four alloys were estimated using the Alstruc code, which is based on standard solidification and diffusion theory and consists of three modules, i.e. solidification, homogenization and an Mg_2Si module [13]–[15].

3.3 Numerical simulations

The work-hardening behaviour of the materials after necking was established by performing finite element (FE) simulations of the tensile tests. The explicit solver of the finite element code LS-DYNA [19] was used to carry out the FE simulations, using four-node quadrilateral axisymmetric elements with one-point quadrature and stiffness-based hourglass control to avoid zero-energy modes. Mass scaling was used to reduce the computation time, and it was checked that the kinetic energy remained negligible compared with the internal energy of the samples during the deformation process. A characteristic element size of 0.15 mm, which gives 20 elements across the radius of the sample, was found to give sufficient accuracy based on a mesh-size sensitivity study.

The materials were modelled using the J_2 flow theory, i.e. the von Mises yield criterion, the associated flow rule and an isotropic hardening rule. The work-hardening curve was described with a two-term Voce rule, i.e.

$$\sigma_{eq} = \sigma_0 + R, \quad R = \sum_{i=1}^{2} R_i, \quad R_i = Q_i \left(1 - \exp\left(-C_i \varepsilon_{eq}\right)\right) \tag{3}$$

where $\sigma_{eq} = \sqrt{\frac{3}{2}\boldsymbol{\sigma}' : \boldsymbol{\sigma}'}$ is the von Mises equivalent stress, $\boldsymbol{\sigma}'$ being the deviatoric stress tensor, and $\varepsilon_{eq} = \int_0^t \sqrt{\frac{2}{3}\mathbf{D}^p : \mathbf{D}^p}\, dt$ is the von Mises equivalent plastic strain. The plastic rate-of-deformation tensor $\mathbf{D}^p$ is defined by the associated flow rule. Further, σ_0 is the yield stress, R_i are the work-hardening variables, and Q_i and C_i are hardening constants. The hardening modulus θ is obtained as

$$\theta \equiv \frac{dR}{d\varepsilon_{eq}} = \sum_{i=1}^{2} \frac{dR_i}{d\varepsilon_{eq}} \tag{4}$$

where

$$\frac{dR_i}{d\varepsilon_{eq}} = C_i Q_i \exp\left(-C_i \varepsilon_{eq}\right) = C_i \left(Q_i - R_i\right), \quad i = 1, 2 \tag{5}$$

Plots of the hardening modulus θ versus the work-hardening variable R will be used in Section 4.2 to assess the work-hardening evolution of the various materials. The constants $\theta_i \equiv C_i Q_i$, $i = 1, 2$, represent the contributions to the initial work-hardening modulus from the two work-hardening terms R_1 and R_2, while Q_i, $i = 1, 2$, are the saturation values of these two terms. The saturation stress obtained at large strains is thus $\sigma_{sat} = \sigma_0 + Q_1 + Q_2$. We will here arrange the terms so that $C_1 \geq C_2$, which implies that the first term R_1 saturates at lower strain than the second term R_2. Accordingly, the parameters Q_1 and C_1 are important for the work-hardening at small and moderate strains, while the parameters Q_2 and C_2 determine the work-hardening at larger strains.

The model parameters were determined using LS-OPT [19], which is an optimization tool that interacts with LS-DYNA. The measured force-diameter reduction curves from the tests were used as target curves, and 20 series with 10 simulations each were run to optimize the parameter sets for each material. A typical force-diameter reduction curve was used for each material as the spread between parallel tests was negligible. Two exceptions were EX materials Al0.2Fe and Al1.2Mn where modest scatter was found. Fitted work-hardening parameters for all materials are compiled in Table 3, which also gives the measured 0.2% proof stress $\sigma_{0.2}$, the mean squared error (MSE) of the fits, and the average failure strain from the tests. In general, the resulting numerical force-diameter reduction curves were in good agreement with the experimental data, as can be seen from the low MSE values in Table 3.

However, some deviation was found at large plastic strains above 100% for the EX and RR materials. Comparisons between experimental and numerical results can be found in [12] for the CH materials, and in [20] for the extruded AlMgSi alloy.

4. Results and discussion

4.1 Initial microstructure

The different processing routes used in this investigation resulted in changes in the microstructure as seen in Figure 2 to Figure 4, showing in turn the grain structure, the particle distribution and the crystallographic texture of the materials. The average spherical grain size was obtained from the EBSD data, where a misorientation of 15° was used to define the high angle grain boundary, and the results are provided in Table 4. The micrographs for the CH materials show an arbitrary plane as the grain and particle structures were assumed random.

The main features of the CH materials were an equiaxed grain structure and an inhomogeneous distribution of the constituent particles [12]. By extruding the alloys a recrystallized grain structure was formed for all the alloys, except for the Al0.8Fe alloy where the grain structure consisted of elongated, deformed grains, see Figure 2. This was most probably caused by the high amount of iron that resulted in a high density of fine secondary iron particles preventing subgrain growth and recrystallization. During extrusion the constituent particles were broken-up and lined up in stringers along the extrusion direction, see Figure 3. The particles were more evenly distributed in the matrix for the EX and RR materials compared to the CH materials, where the constituent particles were mainly located to the grain and dendrite boundaries.

Figure 4 shows the ODFs of the materials. As expected, the CH materials have almost random texture with maximum intensity less than 4. Marked crystallographic texture was formed during extrusion. The recrystallized alloys exhibited mainly cube texture, while Al0.8Fe had fibre texture. The maximum intensity was ranging from about 8 for Al1.2Mn to more than 116 for AlMgSi; i.e., from a rather weak to a very strong texture. Deforming the alloys by cross rolling with subsequent heat treatment, transformed the grain orientation into a nearly random or weak texture for all alloys—the maximum intensity varied from 4 to 8.

4.2 Strength and work-hardening

Figure 5 presents measured σ_t-ε_l curves and predicted σ_{eq}-ε_{eq} curves for all materials and process routes, while Figure 6 gives corresponding θ-R curves. These results were

obtained from Equations (1)–(5) and the parameter sets compiled in Table 3. The curves were stopped at incipient failure in the respective tests, assumed to occur at the maximum true stress in the tensile tests.

The AlMgSi alloy exhibits the highest strength, followed by the Al1.2Mn, Al0.8Fe and Al0.2Fe alloys, in that order, for the CH and RR materials. The EX materials are ordered slightly differently, i.e., the Al0.8Fe and Al1.2Mn alloys have similar strength, with Al0.2Fe as the weakest and AlMgSi as the strongest alloys. The reason for this discrepancy is the non-recrystallized microstructure of the Al0.8Fe alloy that enhances its strength (but decreases its ductility) with respect to the other alloys that are fully recrystallized. The strength and work-hardening of the four alloys are mostly governed by the solute content, while the constituent particles play a less important part. It was found in [12] that Al0.8Fe has a volume fraction of constituent particles that is several times higher than Al0.2Fe, while the solute content is about the same. The effect of this large difference in particle fraction is a rather small increase in strength and initial work-hardening. This conclusion holds only for the CH and RR materials, while the different grain structure of the extruded Al0.2Fe and Al0.8Fe increases the differences between these two materials. The major differences in strength and work-hardening between the four alloys are expected to be caused by elements in solid solution [21], clusters/co-clusters of elements [22], small precipitates [4] and dispersoids [5]. The dispersoids occur here only in the Al1.2Mn alloy. The AlMgSi alloy, which exhibits the highest strength and work-hardening modulus, also has the highest amount of alloying elements in solid solution [12]. The CH materials also contain hardening precipitates due to the slow cooling rate from the homogenization temperature [23], while the EX and RR materials contain clusters of solute elements formed during the natural ageing.

It is further seen in Figure 6 that the $\theta - R$ curve is consistently highest for the AlMgSi alloy, followed by, in turn, Al1.2Mn, Al0.8Fe and Al0.2Fe. This ranking holds from initial yielding until failure for all the three processing routes. These plots also show that in the saturation phase (i.e., for large strains) the work-hardening modulus becomes similar for Al0.2Fe, Al0.8Fe and Al1.2Mn. The $\theta - R$ curves further display two regions with distinct slopes, representing the two terms of the extended Voce rule used to fit the experimental data. The second region is assumed here to represent stage IV work-hardening, where the hardening modulus decreases slowly as the saturation stress is approached. Based on Figure 6 it is found that AlMgSi displays a lower reduction of the hardening modulus in the initial region compared with the other alloys for all microstructures. This is linked to the higher solute content—and possibly also to clusters formed during natural ageing. It is further

interesting to note that the extruded Al0.8Fe alloy, which did not recrystallize during extrusion, has a markedly lower reduction of the hardening modulus in the initial region than the extruded Al0.2Fe and Al1.2Mn alloys. It is even slightly lower than that of the extruded AlMgSi alloy. The reason might be the dislocation network present in the non-recrystallized fibrous grain structure in combination with Fe-clusters/precipitates formed on the dislocation network during and after extrusion preventing dislocation migration.

4.3 Ductility

Typical fracture surfaces of the tensile test specimens are shown in Figure 7. The fracture mode is cup-and-cone in all cases, implying that the fracture started from the centre and grew outward towards the edges. All CH materials and three of the RR materials exhibited isotropic plastic flow, in the sense that the cross section remained circular all the way to fracture. On the contrary, all the EX materials, which were found to have significant texture, cf. Figure 4, clearly exhibited anisotropic plastic flow and the shape of the final cross section varied from elliptic to almost rectangular. The cold rolled and recrystallized Al0.2Fe material had rather weak texture (maximum intensity of 5), but still the cross section developed a diamond shape at large strains. One possible explanation for this rather unexpected result could be the presence of cube and Goss texture. Despite the weak texture, these texture components may persist to large deformations compared to other texture components [24] and may possibly lead to the observed diamond shape. A similar texture is observed for the Al0.8Fe. However, the increased amount of particles in this alloy may be more dominating at large strains. Also noticeable is the spiral form of the fracture surface seen for two of the RR materials.

The difference in ductility between the materials can be roughly judged from the projected areas of the fracture surfaces presented in Figure 7, while the average failure strain based on three parallel tests is given in Table 3. Recall that the failure strain is here defined as the true strain at maximum true stress. It is seen that the failure strain is consistently higher for the EX and RR materials than for the CH materials, while the difference between the ductility of the former two material classes is less clear. In particular, the ductility is about doubled for the AlMgSi alloy after extrusion, while the effect is much less, but still significant, for the other alloys. The improvement of the ductility of the EX materials, as compared with the CH counterparts, is attributed to the breaking-up and spatial re-distribution of the intermetallic particles. These particles are large and located to the grain and dendrite boundaries in the CH materials. The particles are broken-up into smaller pieces during extrusion and aligned in the extrusion direction due to the large plastic deformations, cf. Figure 3. Similar particle sizes

and spatial distributions are found also after the subsequent cold rolling and heat treatment, thus explaining the similar ductility between the EX and RR materials.

Figure 8 shows fractographs of the tensile tests for all materials. In all cases, a ductile fracture mode is apparent and the fracture surface is covered with two categories of dimples, i.e., a low density of coarse dimples and a higher density of small dimples. Coarse constituent particles were seen at the bottom of the dimples, indicating nucleation, growth and coalescence of voids in connection to these particles. The voids were either nucleated around the constituent particles by decohesion or particle cracking [25] or they may be pre-existing in the CH materials [26][27]. Even if particles were not seen in all the coarse dimples, it cannot be excluded that particles have been present; indeed, the particles may have fallen out during fracture or they may be present in the opposite fracture surface. The size and number density of dimples are linked to the size and density of the constituent particles, e.g., Al0.2Fe alloy has fewer but coarser dimples than Al0.8Fe, while Al0.8Fe and Al1.2Mn have approximately the same density of coarse dimples. Small dimples without particles were also observed in the fracture surface, indicating other possible mechanisms for void coalescence, such as interacting slip planes creating voids in the junction points [28].

Figure 9 displays longitudinal sections from the centre of the fractured tensile samples for the AlMgSi alloy. In the CH materials, large voids are seen immediately in front of the fracture surface and the fracture surface is also rougher than for the EX and RR materials. In addition, small voids adjacent to the particles or in-between two particles were seen for the CH materials, which were not observed in the EX and RR materials. This may indicate that the voids found in the CH materials prior to testing, cf. [12], have been closed during the extrusion. If this is the case, it would contribute to the increased ductility observed after extrusion. Similar observations were made also for the other alloys. A detailed discussion on the fracture mechanisms in the CH materials can be found in Westermann et al. [12].

Figure 10 shows the failure strain ε_f plotted against the yield stress $\sigma_{0.2}$ of the materials. The failure strain is found to decrease consistently and approximately linearly with the yield stress for similar microstructure, i.e., either CH, EX or RR materials with fully recrystallized grain structure. Similar results were reported in [29] and [30]. The reduction in ductility with strength is found to be less for the RR materials than for the CH and EX materials. Note that the extruded Al0.8Fe material is excluded from the linear interpolation for the EX materials because of the different microstructure. Due to the non-recrystallized microstructure, the

strength is higher and the ductility lower than what would be expected if the material was recrystallized.

4.4 Uncertainties in the experimental-numerical method

There are some important uncertainties in the experimental-numerical method used to extract the equivalent stress-strain curves from the test data.

The constitutive model assumes isotropic plasticity depending only on the second invariant of the stress deviator. It is assumed that this is a reasonable assumption for the CH and RR materials that exhibited isotropic plastic flow, but it may be doubtful for the EX materials and the cold rolled and recrystallized Al0.2Fe that behaved strongly anisotropic. In [31], an anisotropic plasticity model was used in the optimization procedure to account for the initial anisotropy at the cost of a considerable increase in the computation time. The results obtained with J2 flow theory for a textured alloy were also evaluated in [31] and it was found that there was a noticeable effect on the equivalent stress-strain curve.

During large-strain deformation in tension, the grains become elongated and crystallographic texture develops in the necked region that might lead to plastic anisotropy in initially isotropic materials and evolution of plastic anisotropy in initially textured materials. In the finite element simulations of the tension test, the materials were assumed to remain isotropic to failure. At the cost of increasing the computation time by several orders of magnitude, it would probably be possible to use polycrystal plasticity simulations in the optimization procedure and thus include both initial and strain-induced plastic anisotropy. An indication of the texture evolution is obtained by considering the strain ratio, which is here defined as the ratio of the two transverse strains measured in the neck. The strain ratios are plotted for the Al1.2Mn alloy in Figure 11. As expected, the initial strain ratio equals unity for the CH material with nearly random texture and remains unchanged to failure owing to the symmetry of the loading conditions. After extrusion, the strain ratio deviates from unity and exhibits some evolution due to the initial and evolving anisotropy. The cross rolling and the subsequent recrystallization reduce the anisotropy (cf. Figure 4) and the strain ratio is again rather close to unity and remains practically constant. Comparable results were found also for the other alloys.

Another source of error in the experiments is the calculation of the current area based on the measurements of the diameters along the principal axes of orthotropy. Equation (2) is only correct for specimens either retaining the circular shape of the minimum cross section or developing an elliptic shape due to plastic anisotropy. Figure 7 shows that this is not the case

for a couple of the EX and one of the RR materials. Since the shape of the cross section develops with strain, the error in the estimated area also increases towards fracture. To assess the error, the projected areas of the fracture surfaces shown in Figure 7 were measured from the images and the associated fracture strain compared with the fracture strain found from the laser measurements. It is noted here that the fracture strain is defined as the logarithmic strain at complete fracture of the specimen (i.e., at zero true stress), whereas the failure strain, herein denoted ε_f, is the logarithmic strain at the maximum value of the true stress. The results are presented in Figure 12 and found reasonably consistent. The failure strain is always less than the fracture strain, either obtained by area or laser measurements, and further the area measurements give consistently higher values than the laser measurements. The latter observation is reasonable since it is not an easy task to follow the minimum cross section with the laser during the softening branch of the true stress-strain curve. Figure 12 also illustrates clearly that a significant part of the strain to fracture occurs in the softening branch of the true stress-strain curve, which is assumed to be caused by void coalescence. Another issue here is that the assumption of isochoric plastic flow is hardly valid in the softening branch of the true stress-strain curve where dilation occurs due to the void growth and coalescence.

After necking, the strain rate inside the necked region increases, since the tests were conducted with constant cross-head velocity. This increase is nearly linear and at failure the strain rate is between one and two order of magnitudes higher than the initial one, depending on the ductility of the material at hand. Strain-rate sensitivity is neglected in the constitutive model and thus the apparent work-hardening may partly be caused by an increased flow stress due to rate sensitivity. This effect would become stronger with strain since the strain rate increases almost linearly with the strain in the neck. Since the rate sensitivity of the actual alloys has not been determined experimentally, the potential error introduced by disregarding the increasing strain rate cannot be quantified. It was shown in [32] that the alloys AA1200 and AA3103 exhibit noticeable rate sensitivity and thus this issue should be investigated further. However, other alloys, namely AA6060 and AA6082 in T6 condition, were shown in [33] to be practically insensitive to strain rate at room temperature, while weak rate sensitivity was found for AA7003 and AA7108 in T6 condition.

5. Conclusions

The strength, work-hardening and ductility of four aluminium alloys exposed to three different processing steps were studied by conducting tensile tests on axisymmetric specimens, using an experimental-numerical method to extract the equivalent stress-strain

curves after necking and up to failure. The method is based on using two perpendicular lasers to measure the minimum cross section of the specimen and finite element simulations to extract the equivalent stress using a nonlinear optimization technique.

The experimental-numerical results showed that the strength and work-hardening of the alloys were primarily controlled by the solute content but with some significant contributions also of the constituent particles and the grain structure. Given a fully recrystallized grain structure, the strength and work-hardening increased consistently with increasing solute content. However, based on the results obtained for the two AlFe alloys, it is concluded that the fraction of large intermetallic particles had a significant contribution to the strength and the initial work-hardening, and further that a non-recrystallized grain structure led to a markedly stronger material with greater work-hardening and lower ductility than the recrystallized grain structure.

The failure strain was found to decrease linearly with increasing strength of the material for a given microstructure. It was further observed that processing by extrusion consistently increased the ductility of the materials, and for the AlMgSi material the strain to failure was roughly doubled. In most cases, the subsequent cold rolling and heat treatment did not substantially change the ductility. The enhancement of ductility of the extruded materials, as compared with the cast and homogenized materials, was attributed to the breaking-up and spatial re-distribution of the intermetallic particles. In the cast and homogenized materials, these particles are large and situated on the grain and dendrite boundaries. During extrusion, the particles are broken-up into smaller pieces and aligned in the extrusion direction due to the large plastic deformations. Similar particle sizes and spatial distributions were found in the cold rolled and recrystallized materials.

It is believed that the experimental-numerical method used in this study has great potential in establishing more reliable work-hardening and fracture models for aluminium alloys since accurate experimental tensile data are acquired up to fracture. However, the method could be improved by accounting for plastic anisotropy at the cost of increasing the computing time of the optimization procedure.

Acknowledgement

The financial support of this work from the Structural Impact Laboratory (SIMLab), Centre for Research-based Innovation (CRI) at the Norwegian University of Science and Technology (NTNU), is gratefully acknowledged.

References

[1] D.J. Lloyd. The work hardening of some commercial Al alloys. Material Science Forum 519-522 (2006) 55–62.

[2] L.M. Cheng, W.J. Poole, J.D. Embury, D.J. Lloyd. The influence of precipitation on the work-hardening behavior of the aluminum alloys AA6111 and AA7030. Metallurgical and Materials Transactions 34A (2003) 2473–2481.

[3] J.D. Embury, W.J. Poole, D.J. Lloyd. The work hardening of single phase and multi-phase aluminum alloys. Materials Science Forum 519-521 (2006) 71–78.

[4] O.R. Myhr, Ø. Grong, K.O. Pedersen. A combined precipitation, yield strength, and work hardening model for Al-Mg-Si alloys. Metallurgical and Materials Transactions 41A (2010) 2276–2289.

[5] Q. Zhao, B. Holmedal, Y. Li. Influence of dispersoids on microstructure evolution and work hardening of aluminium alloys during tension and cold rolling. Philosophical Magazine 93 (2013) 2995–3011.

[6] D. Dumont, A. Deschamps, Y. Brechet. On the relationship between microstructure, strength and toughness in AA7050 aluminum alloy. Materials Science and Engineering A 356 (2003) 326–336.

[7] T. Morgeneyer, M.J. Starink, I. Sinclair. Evolution of voids during ductile crack propagation in an aluminium alloy sheet toughness test studied by synchrotron radiation computed tomography. Acta Materialia 56 (2008) 1671–1679.

[8] D. Steglich, W. Brocks, J. Heerens, T. Pardoen. Anisotropic ductile fracture of Al 2024 alloys. Engineering Fracture Mechanics 75 (2008) 3692–3706.

[9] J.B. Jordon, M.F. Horstemeyer, K. Solanki, J.D. Bernard, J.T. Berry, T.N. Williams. Damage characterization and modeling of a 7075-T651 aluminum plate. Materials Science and Engineering A 527 (2009) 169–178.

[10] Y. Chen, K.O. Pedersen, A.H. Clausen, O.S. Hopperstad. An experimental study on the dynamic fracture of extruded AA6xxx and AA7xxx aluminium alloys. Materials Science and Engineering A523 (2009) 253–262.

[11] K.O. Pedersen, T. Børvik, O.S. Hopperstad. Fracture mechanisms of aluminium alloy AA7075-T651 under various loading conditions. Materials and Design 32 (2011) 97–107.
[12] I. Westermann, K.O. Pedersen, T. Furu, T. Børvik, O.S. Hopperstad. Effects of particles and solutes on the strength, work-hardening and ductile fracture of aluminium alloys. Mechanics of Materials 79 (2014) 58–72.
[13] A.L. Dons, E.K. Jensen, Y. Langsrud, E. Trømborg, S. Brusethaug. The Alstruc microstructure solidification model for industrial aluminum alloys. Metallurgical and Materials Transactions 30A (1999) 2135–2146.
[14] A.L. Dons. The Alstruc homogenization model for industrial aluminum alloys. Journal of Light Metals 1 (2001) 133–149.
[15] J. Røyset, E.B. Bjørnbakk, T. Nyborg, O. Reiso, J.A. Sæter, U. Tundal, A.L. Dons, T. Hagelien. Almech – a computer program for alloy selection and extrusion process improvement. Proceedings of the 8th International Aluminium Extrusion Technology Seminar, Orlando, Florida, pp. 81–91, 2004.
[16] I. Westermann, O.S. Hopperstad, K. Marthinsen, B. Holmedal. Ageing and work-hardening behaviour of a commercial AA7108 aluminium alloy. Materials Science and Engineering A 524 (2009) 151–157.
[17] C. Mondal, A.K. Singh, A.K. Mukhopadhyay, K. Chattopadhyay. Tensile flow and work hardening behavior of hot cross-rolled AA7010 aluminum alloy sheets. Materials Science and Engineering A 577 (2013) 87–100.
[18] T. Furu, K.O. Pedersen. The influence of grain structure and texture on formability and toughness of extruded aluminium alloys. Materials Science Forum 519-521 (2006) 1421–1428.
[19] LSTC Livermore Software Technology Corporation. http://www.lstc.com/ [cited: 03.11.14].
[20] O.S. Hopperstad, I. Westermann, K.O. Pedersen, T. Furu, T. Børvik. Influence of processing route on the work-hardening and ductile fracture of an AA6060 aluminium alloy. Materials Science Forum 794-796 (2014) 284–289.
[21] Ø. Ryen, O. Nijs, E. Sjölander, B. Holmedal, H.-E. Ekström, E. Nes. Strengthening mechanisms in solid solution aluminum alloys. Metallurgical and Materials Transactions 37A (2006) 1999–2006.
[22] M.J. Starink, L.F. Cao, P.A. Rometsch. A model for the thermodynamics of and strengthening due to co-clusters in Al–Mg–Si-based alloys. Acta Materialia 60 (2012) 4194–4207.

[23] Y. Birol. Precipitation during homogenization cooling in AlMgSi alloys. Transactions of Nonferrous Metals Society of China 23 (2013) 1875–1881.
[24] F.J. Humphreys, M. Hatherly. Recrystallization and related annealing phenomena. Second edition 2004, Elsevier.
[25] E. Maire, S. Zhou, J. Adrien, M. Dimichiel. Damage quantification in aluminium alloys using in situ tensile tests in X-ray tomography. Engineering Fracture Mechanics 78 (2011) 2679–2690.
[26] J. Campbell. The origin of Griffith cracks. Metallurgical and Materials Transactions 42B (2011) 1091–1097.
[27] H. Toda, H. Oogo, K. Horikawa, K. Uesugi, A. Takeuchi, Y. Suzuki, M. Nakazawa, Y. Aoki, M. Kobayashi. The true origin of ductile fracture in aluminum alloys. Metallurgical and Materials Transactions 45A (2014) 765–776.
[28] K.O. Pedersen, H.J. Roven, O.-G. Lademo, O.S. Hopperstad. Strength and ductility of aluminium alloy 7030. Materials Science and Engineering A 473 (2008) 81–89.
[29] D.J. Lloyd. The scaling of the tensile ductile fracture strain with yield strength in Al alloys. Scripta Materialia 48 (2003) 341–344.
[30] G. Liu, S. Scudino, R. Li, U. Kühn, J. Sun, J. Eckert. Coupling effect of primary voids and secondary voids on the ductile fracture of heat-treatable aluminum alloys. Mechanics of Materials 43 (2011) 556–566.
[31] M. Khadyko, S. Dumoulin, T. Børvik, O.S. Hopperstad. An experimental-numerical method to determine the work-hardening of anisotropic ductile materials at large strains. International Journal of Mechanical Sciences 88 (2014) 25–36.
[32] O.-G. Lademo, O. Engler, J. Aegerter, T. Berstad, A. Benallal, O.S. Hopperstad. Strain-rate sensitivity of aluminum alloys AA1200 and AA3103. Journal of Engineering Materials and Technology 132 (2010) p. 041007 (8 pp.).
[33] Y. Chen, A.H. Clausen, O.S. Hopperstad, M. Langseth. Stress–strain behaviour of aluminium alloys at a wide range of strain rates. International Journal of Solids and Structures 46 (2009) 3825–3835.

List of tables

Table 1. Composition in wt% of the four alloys. Grain refiner (TiB) was added to all alloys in order to obtain a homogeneous grain structure.

Table 2. Homogenization procedure for the different materials.

Table 3. Yield strength and work-hardening parameters of the four alloys after the three processing routes, mean squared error (MSE) from the parameter optimization, and average failure strain from tests.

Table 4. Average grain size in μm.

Tables

Table 1. Composition in wt% of the four alloys. Grain refiner (TiB) was added to all alloys in order to obtain a homogeneous grain structure.

Material	Fe	Mn	Mg	Si	Al
Al0.2Fe	0.2	–	–	0.05	Bal.
Al0.8Fe	0.8	–	–	0.05	Bal.
Al1.2Mn	0.2	1.2	–	0.05	Bal.
AlMgSi	0.2	–	0.5	0.4	Bal.

Table 2. Homogenization procedure for the different materials.

Material	Heating rate [°C/h]	Holding temp. [°C]	Holding time [h]	Cooling rate to RT [°C/h]
Al0.2Fe	100	580	5	200
Al0.8Fe	100	580	5	200
Al1.2Mn	100	600	5	200
AlMgSi	100	585	2.5	300

Table 3. Yield strength and work-hardening parameters of the four alloys after the three processing routes, mean squared error (MSE) from the parameter optimization, and average failure strain from tests.

Cast and homogenized materials								
Material	σ_0 [MPa]	Q_1 [MPa]	C_1	Q_2 [MPa]	C_2	$\sigma_{0.2}$ [MPa]	MSE	$\bar{\varepsilon}_f$
Al0.2Fe	24.37	31.46	32.55	97.26	1.90	26.72	$2.14 \cdot 10^{-6}$	1.574
Al0.8Fe	30.68	37.93	35.58	95.24	2.15	33.69	$2.44 \cdot 10^{-6}$	1.357
Al1.2Mn	39.51	51.40	35.69	106.22	2.16	43.51	$3.25 \cdot 10^{-6}$	1.237
AlMgSi	66.26	62.00	32.36	126.46	4.21	71.21	$1.70 \cdot 10^{-6}$	0.662
Extruded materials								
Material	σ_0 [MPa]	Q_1 [MPa]	C_1	Q_2 [MPa]	C_2	$\sigma_{0.2}$ [MPa]	MSE	$\bar{\varepsilon}_f$
Al0.2Fe	26.76	34.03	31.69	99.09	0.86	29.02	$2.50 \cdot 10^{-5}$	2.154
Al0.8Fe	44.61	51.98	19.88	95.13	1.34	46.89	$5.57 \cdot 10^{-5}$	1.547
Al1.2Mn	37.87	54.38	35.00	109.47	1.25	41.82	$1.17 \cdot 10^{-5}$	1.652
AlMgSi	70.86	118.96	19.57	87.49	0.92	75.59	$4.90 \cdot 10^{-5}$	1.336
Cold rolled and recrystallized materials								
Material	σ_0 [MPa]	Q_1 [MPa]	C_1	Q_2 [MPa]	C_2	$\sigma_{0.2}$ [MPa]	MSE	$\bar{\varepsilon}_f$
Al0.2Fe	28.26	28.05	37.31	86.26	2.41	30.69	$3.60 \cdot 10^{-5}$	1.766
Al0.8Fe	40.96	31.50	37.79	97.89	2.22	43.69	$6.60 \cdot 10^{-6}$	1.713
Al1.2Mn	51.15	48.51	27.98	115.49	1.77	54.20	$1.75 \cdot 10^{-5}$	1.531
AlMgSi	85.03	92.33	19.03	124.04	2.73	89.15	$4.02 \cdot 10^{-6}$	1.279

Table 4. Average grain size in μm.

Material	Cast and homogenized	Extruded	Cold rolled and recrystallized
Al0.2Fe	61	46	43
Al0.8Fe	54	—	25
Al1.2Mn	57	59	28
AlMgSi	66	59	43

List of figures

Figure 1. Sketch of material processing steps after casting: homogenization, extrusion, and rolling and recrystallization.

Figure 2. Optical micrographs of the grain structure for all materials. ND/TD implies that the exact radial direction in the ND/TD plane is not known due to the cold rolling after extrusion.

Figure 3. Particle distribution for all materials obtained in BSE mode in SEM. ND/TD implies that the exact radial direction in the ND/TD plane is not known due to the cold rolling after extrusion.

Figure 4. Orientation distribution function (ODF) for all materials. The sections in Euler angle space $(\varphi_1, \Phi, \varphi_2)$ are presented at $\varphi_2 = 0^\circ, 5^\circ, ..., 90^\circ$. The level curves are shown at intensities 1, 2, 4, 8, 16, … times random and the maximum intensity is given for each material.

Figure 5. Plots of measured σ_t - ε_l curves (left) and predicted σ_{eq} - ε_{eq} curves (right) for all materials and process routes. All curves are stopped at failure in the respective uniaxial tensile tests, assumed to occur at maximum true stress.

Figure 6. Plots of θ - R curves for all materials and process routes. All curves are stopped at failure in the respective uniaxial tensile tests, assumed to occur at maximum true stress.

Figure 7. Fracture surfaces for all materials obtained in SEM. ND/TD (or TD/ND) implies that the exact radial direction in the ND/TD (or TD/ND) plane is not known due to the cold rolling after extrusion.

Figure 8. SEM fractographs for all materials. ND/TD (or TD/ND) implies that the exact radial direction in the ND/TD (or TD/ND) plane is not known due to the cold rolling after extrusion.

Figure 9. Cross sections from the centre of the fractured AlMgSi tensile samples obtained in BSE mode in SEM. TD/ND implies that the exact radial direction in the TD/ND plane is not known due to the cold rolling after extrusion.

Figure 10. Failure strain ε_f versus yield stress $\sigma_{0.2}$ for all materials and tests.

Figure 11. Strain ratio (*r*-value) versus logarithmic (true) strain for the Al1.2Mn material. The results from three parallel tests are shown.

Figure 12. Comparison of failure and fracture strains from laser measurements with fracture strains from area measurements obtained with a microscope on the failed samples. All strains are logarithmic.

Figures

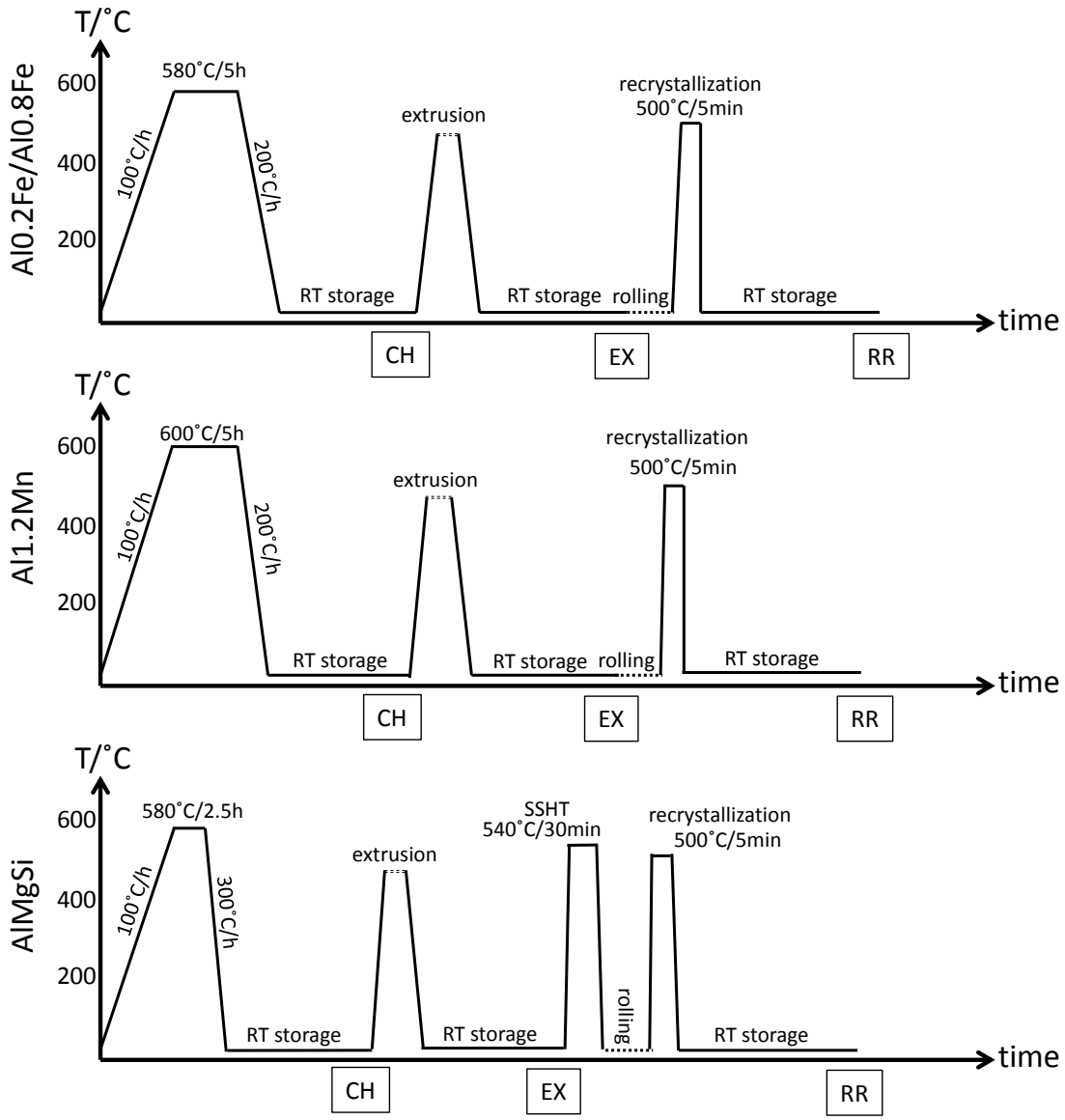

Figure 1. Sketch of material processing steps after casting: homogenization, extrusion, and rolling and recrystallization.

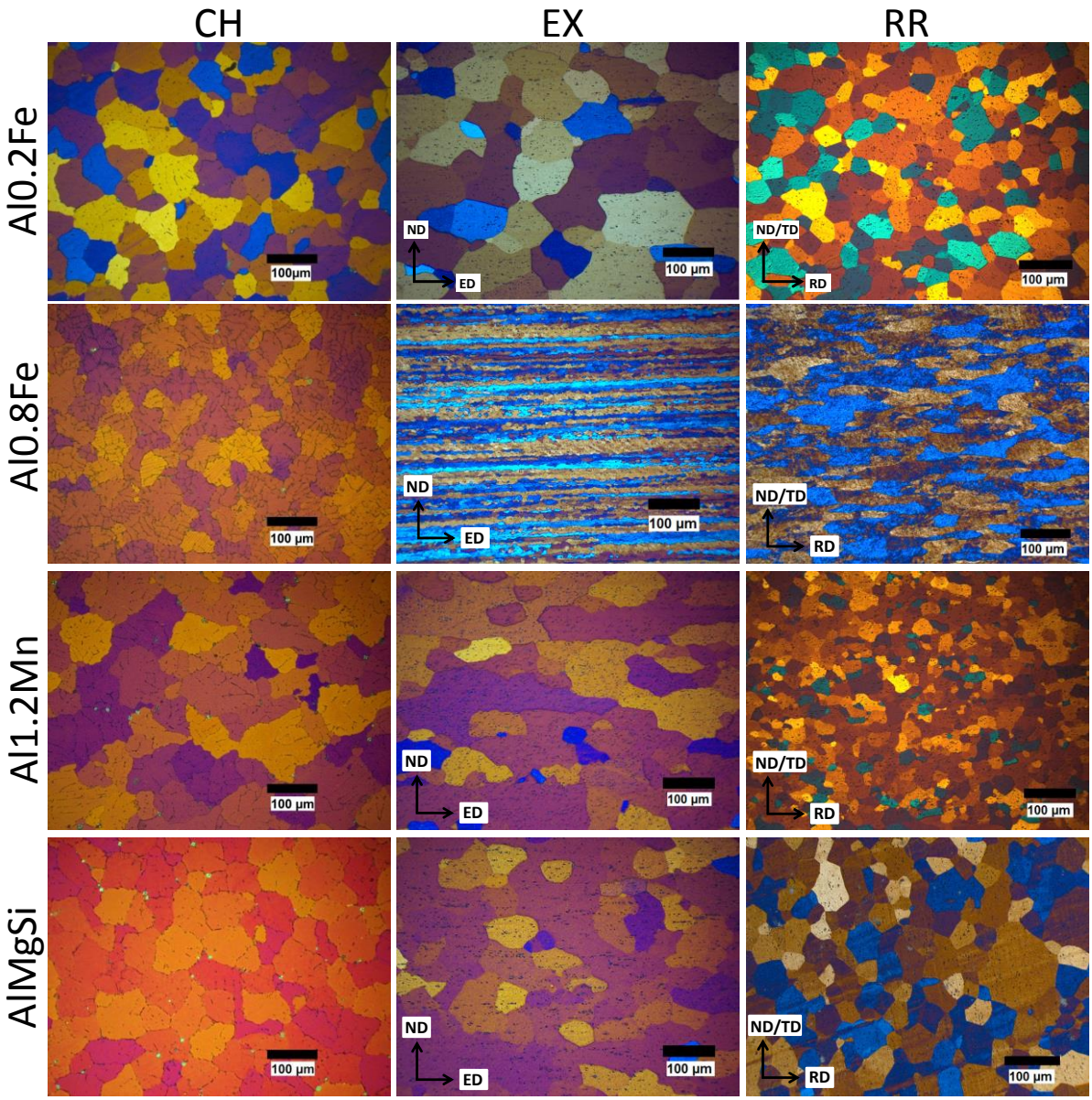

Figure 2. Optical micrographs of the grain structure for all materials. ND/TD implies that the exact radial direction in the ND/TD plane is not known due to the cold rolling after extrusion.

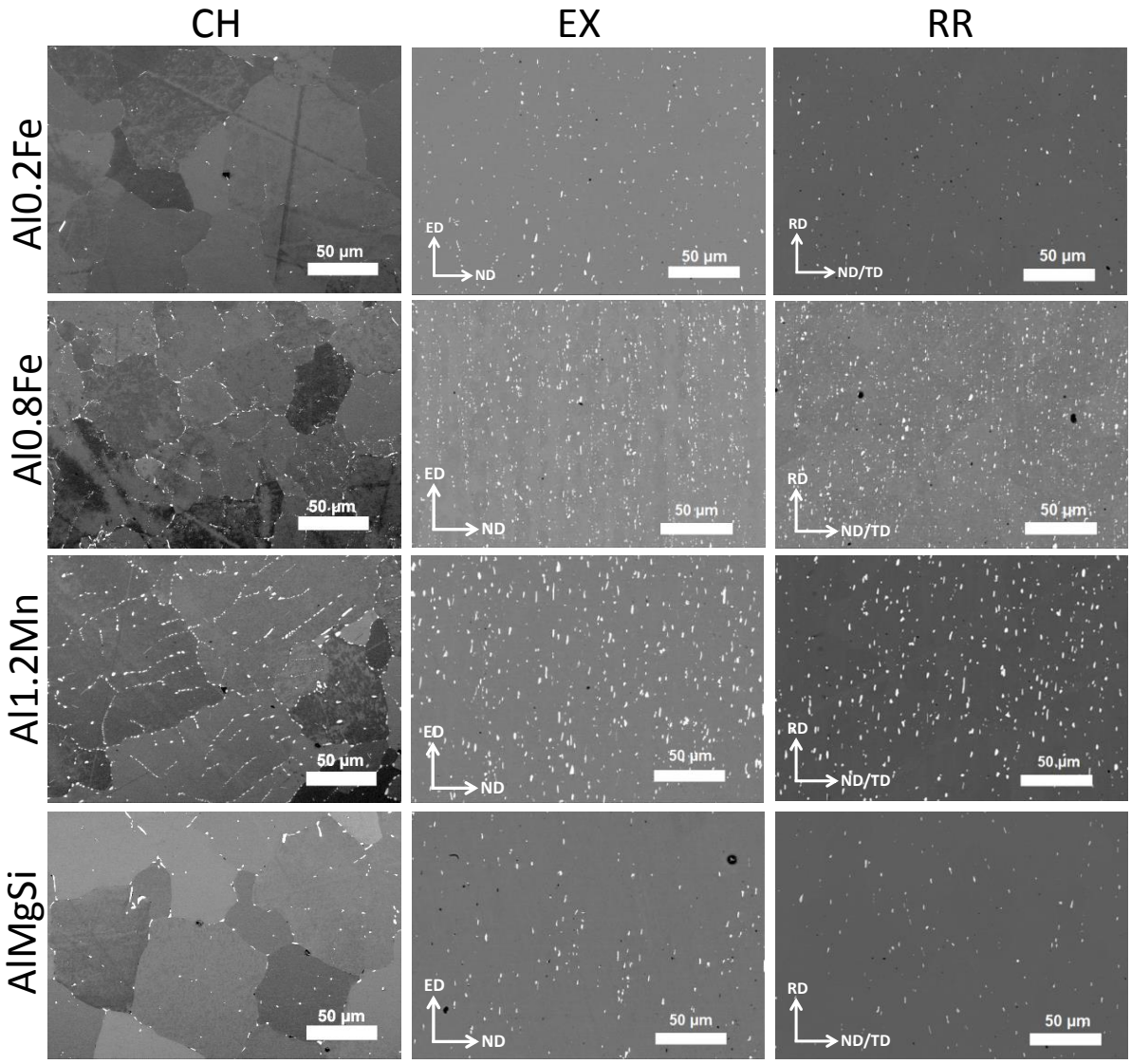

Figure 3. Particle distribution for all materials obtained in BSE mode in SEM. ND/TD implies that the exact radial direction in the ND/TD plane is not known due to the cold rolling after extrusion.

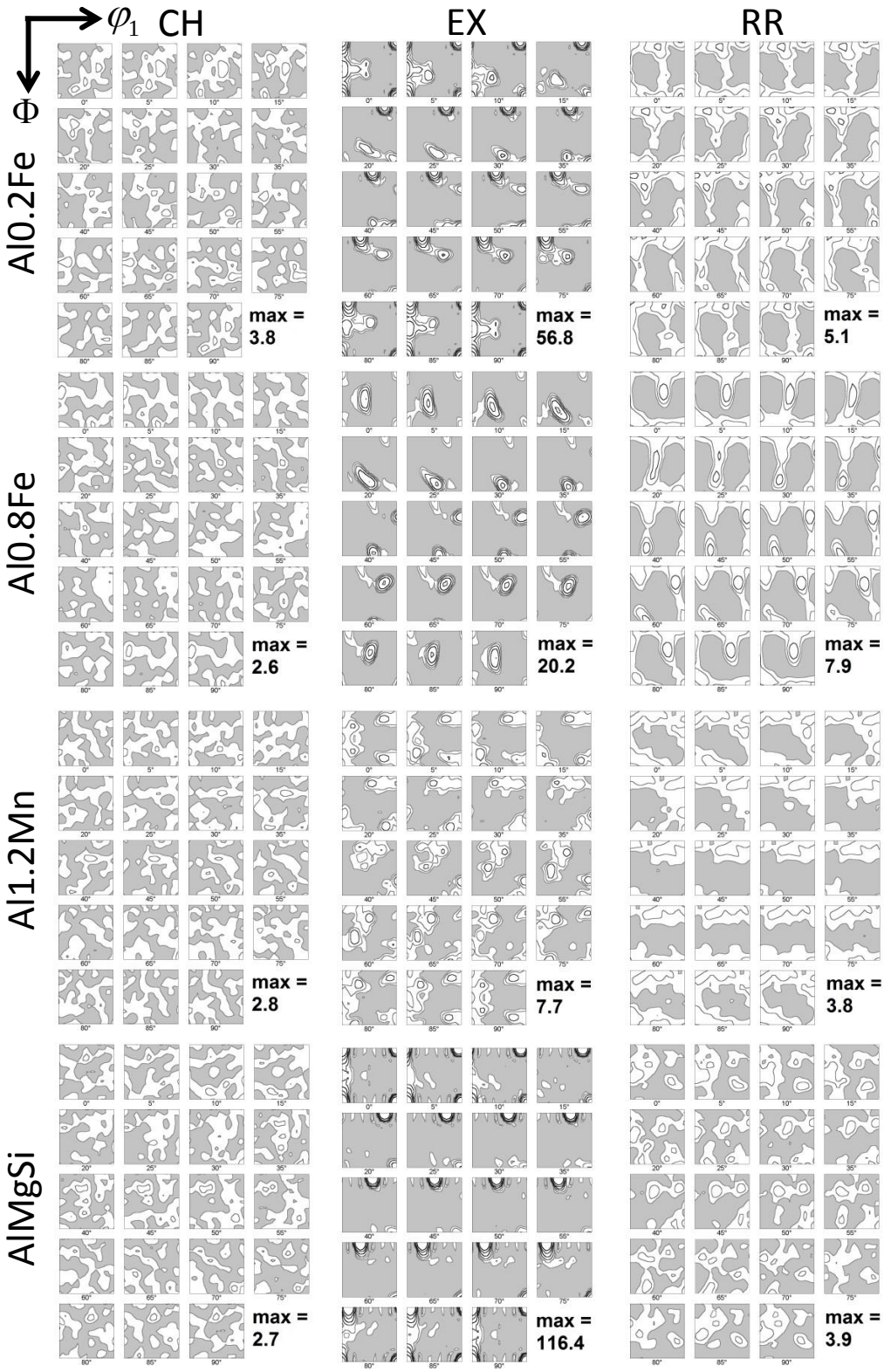

Figure 4. Orientation distribution function (ODF) for all materials. The sections in Euler angle space $(\varphi_1, \Phi, \varphi_2)$ are presented at $\varphi_2 = 0^\circ, 5^\circ, ..., 90^\circ$. The level curves are shown at intensities 1, 2, 4, 8, 16, … times random and the maximum intensity is given for each material.

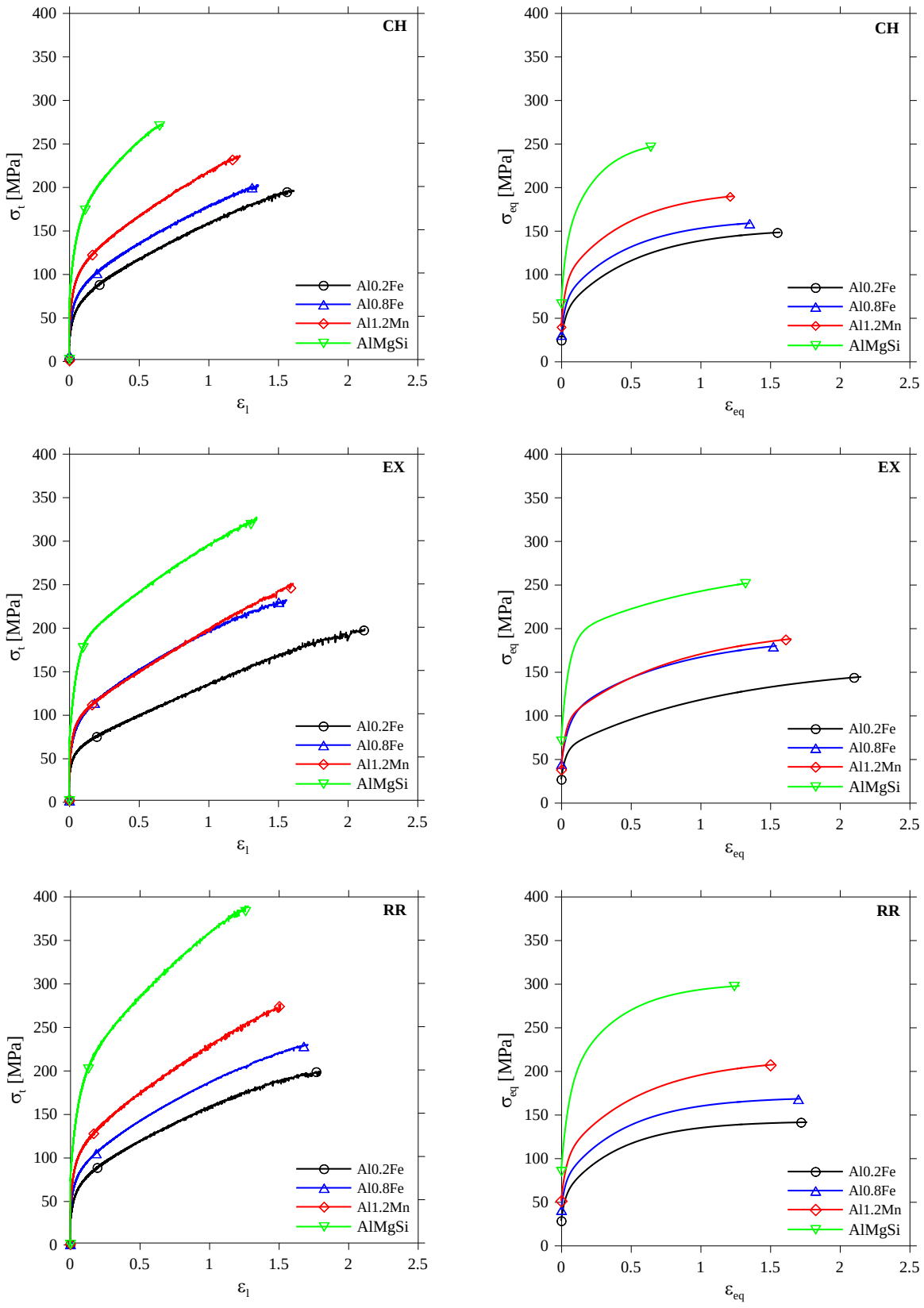

Figure 5. Plots of measured σ_t-ε_l curves (left) and predicted σ_{eq}-ε_{eq} curves (right) for all materials and process routes. All curves are stopped at failure in the respective uniaxial tensile tests, assumed to occur at maximum true stress.

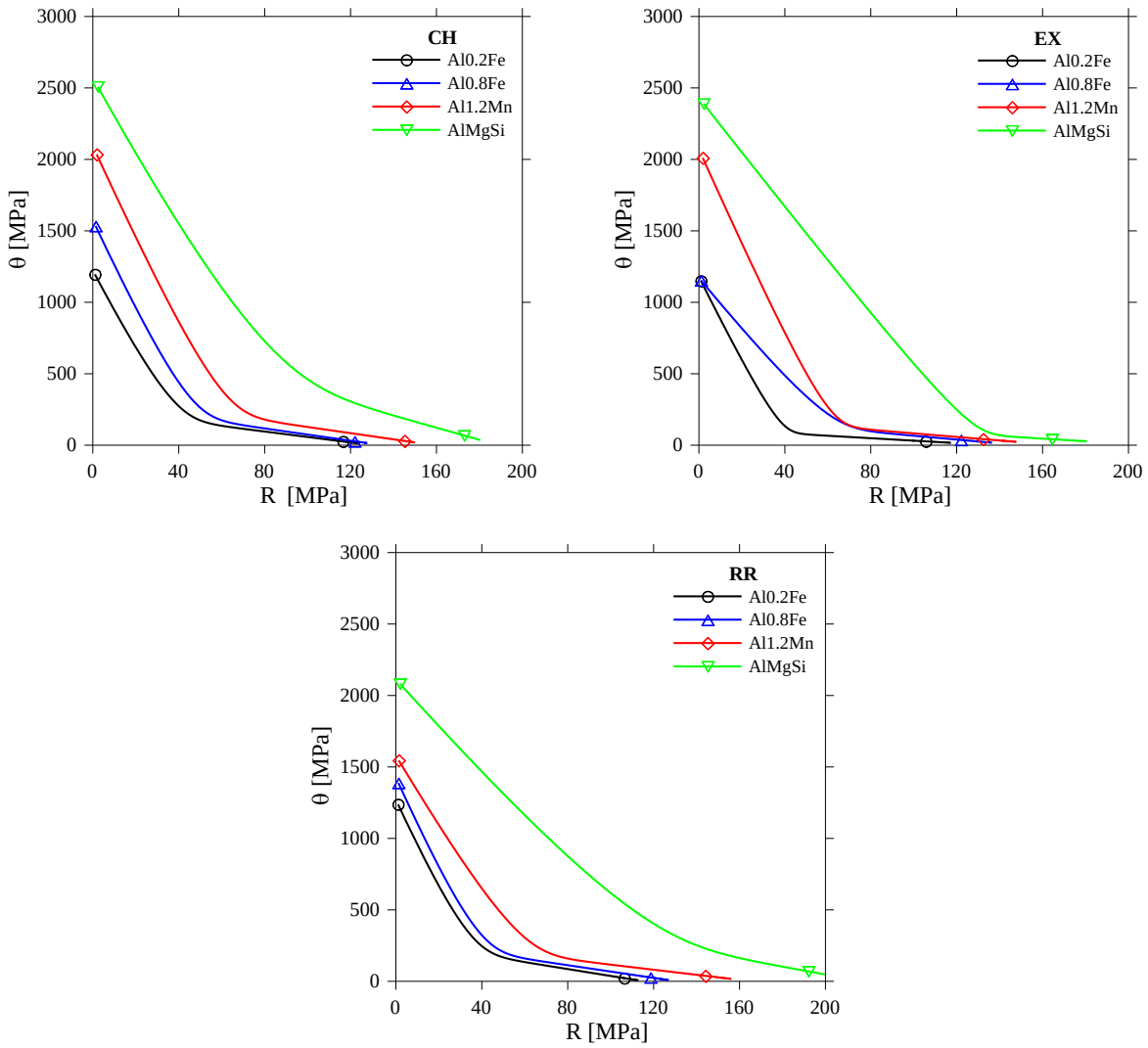

Figure 6. Plots of θ-R curves for all materials and process routes. All curves are stopped at failure in the respective uniaxial tensile tests, assumed to occur at maximum true stress.

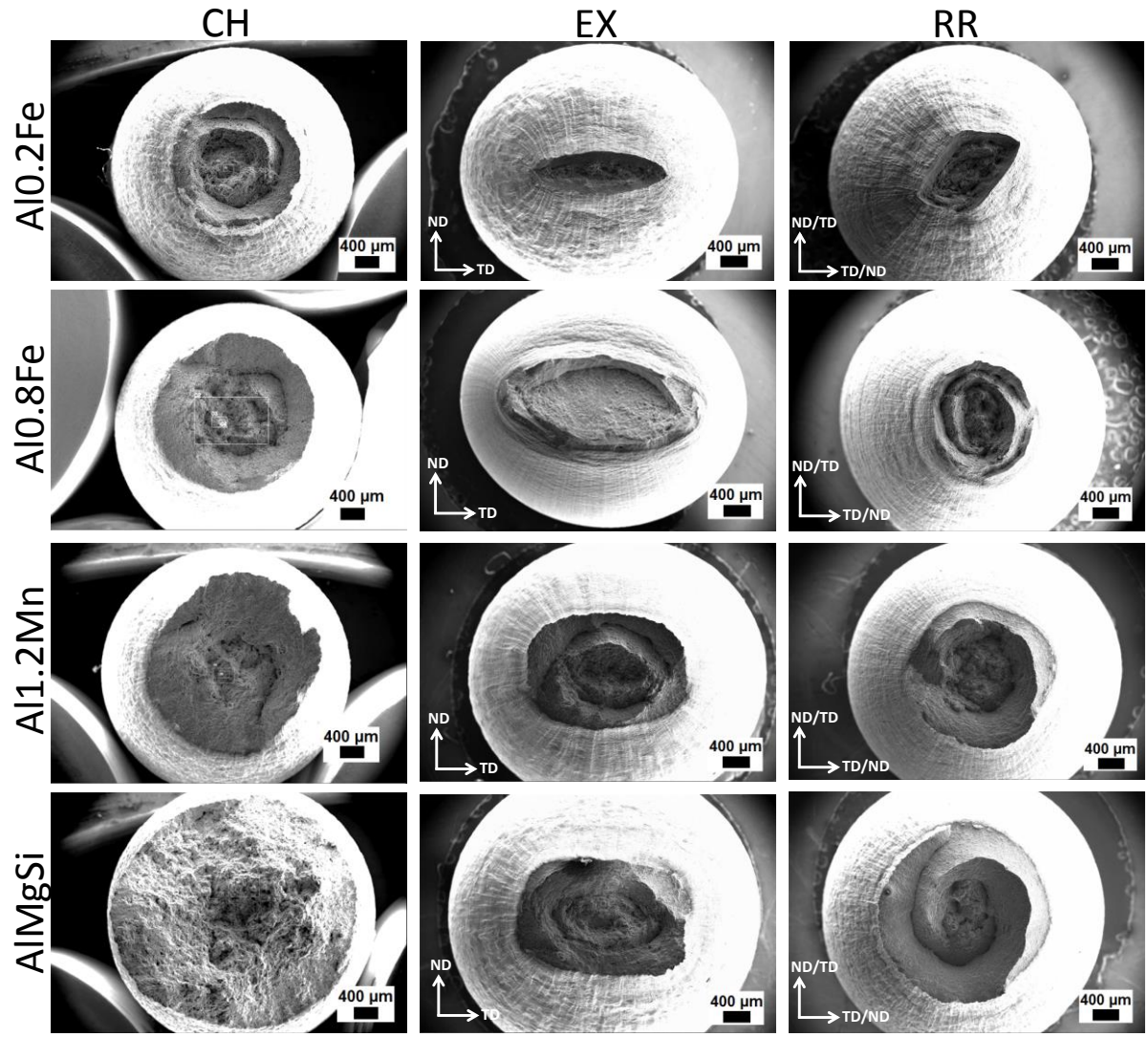

Figure 7. Fracture surfaces for all materials obtained in SEM. ND/TD (or TD/ND) implies that the exact radial direction in the ND/TD (or TD/ND) plane is not known due to the cold rolling after extrusion.

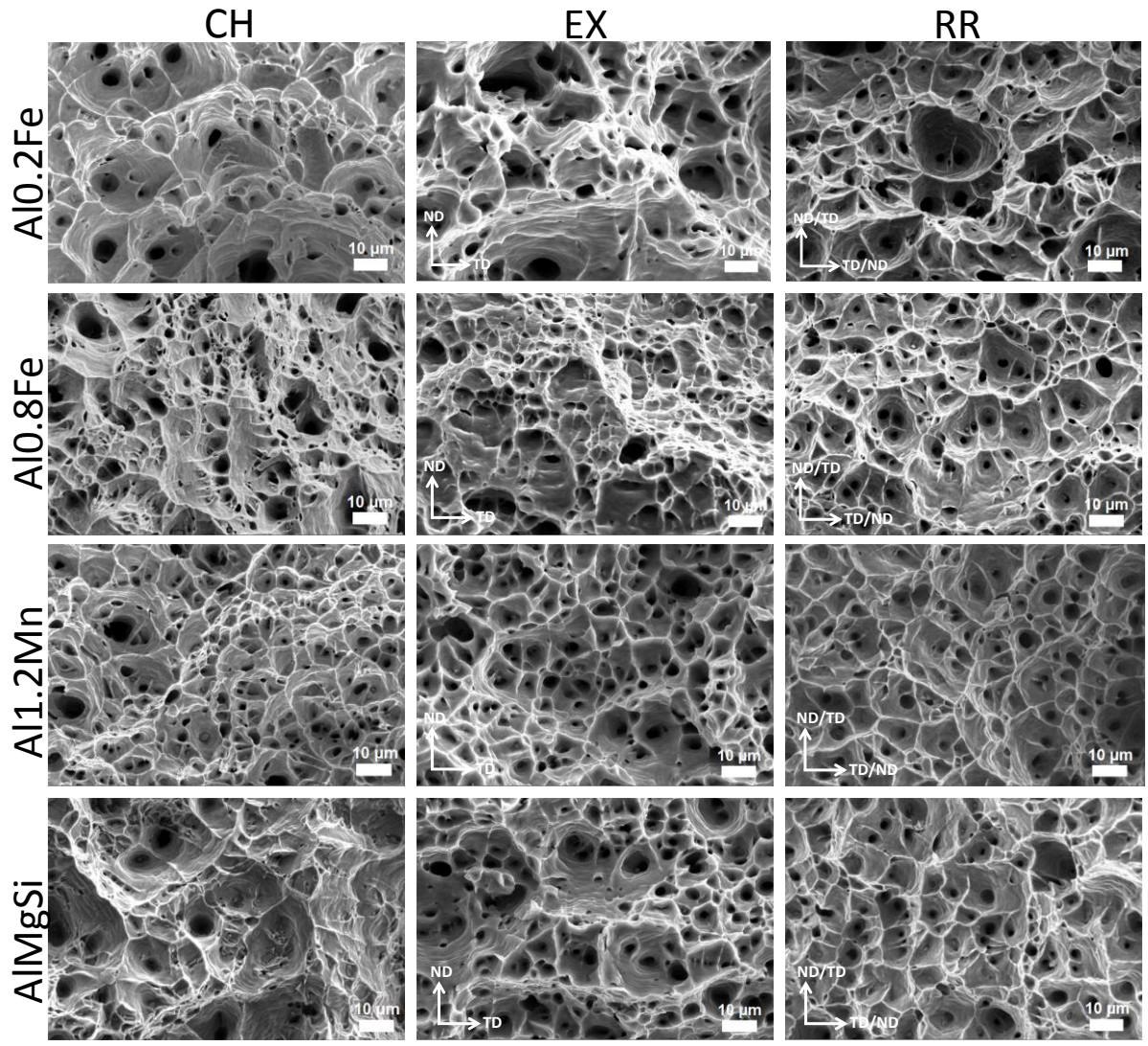

Figure 8. SEM fractographs for all materials. ND/TD (or TD/ND) implies that the exact radial direction in the ND/TD (or TD/ND) plane is not known due to the cold rolling after extrusion.

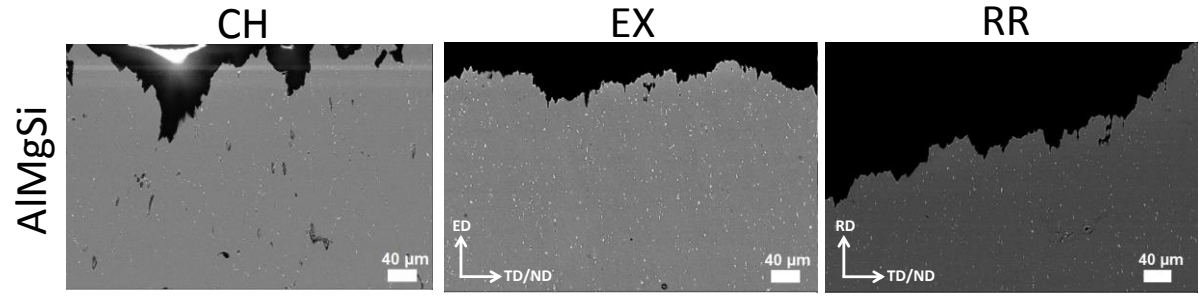

Figure 9. Cross sections from the centre of the fractured AlMgSi tensile samples obtained in BSE mode in SEM. TD/ND implies that the exact radial direction in the TD/ND plane is not known due to the cold rolling after extrusion.

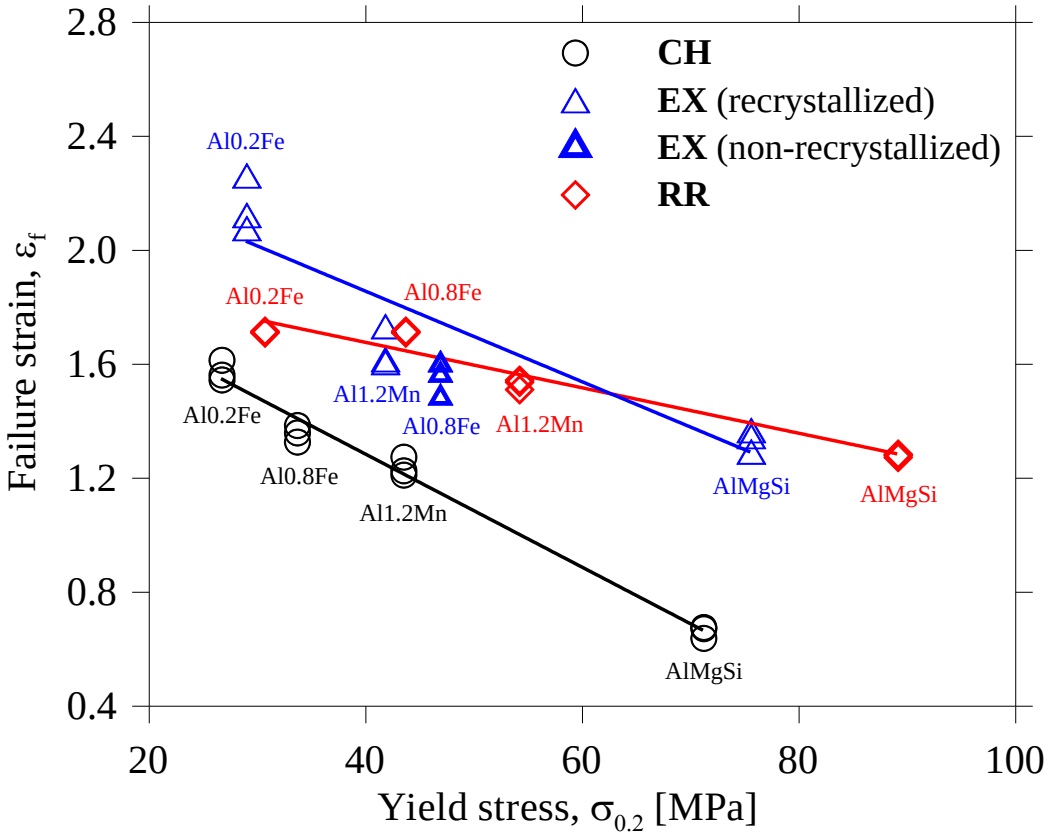

Figure 10. Failure strain ε_f versus yield stress $\sigma_{0.2}$ for all materials and tests.

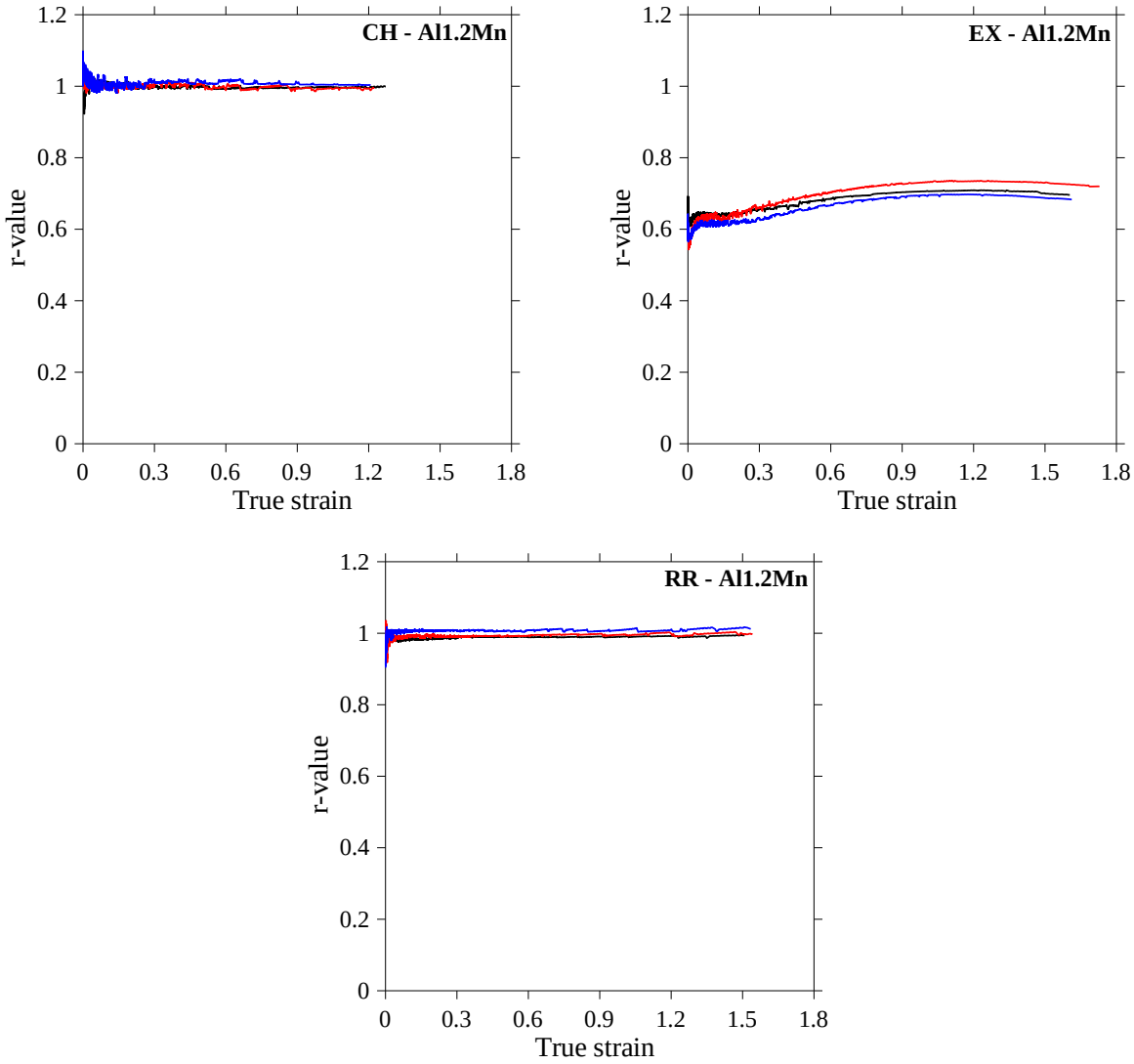

Figure 11. Strain ratio (*r*-value) versus logarithmic (true) strain for the Al1.2Mn material. The results from three parallel tests are shown.

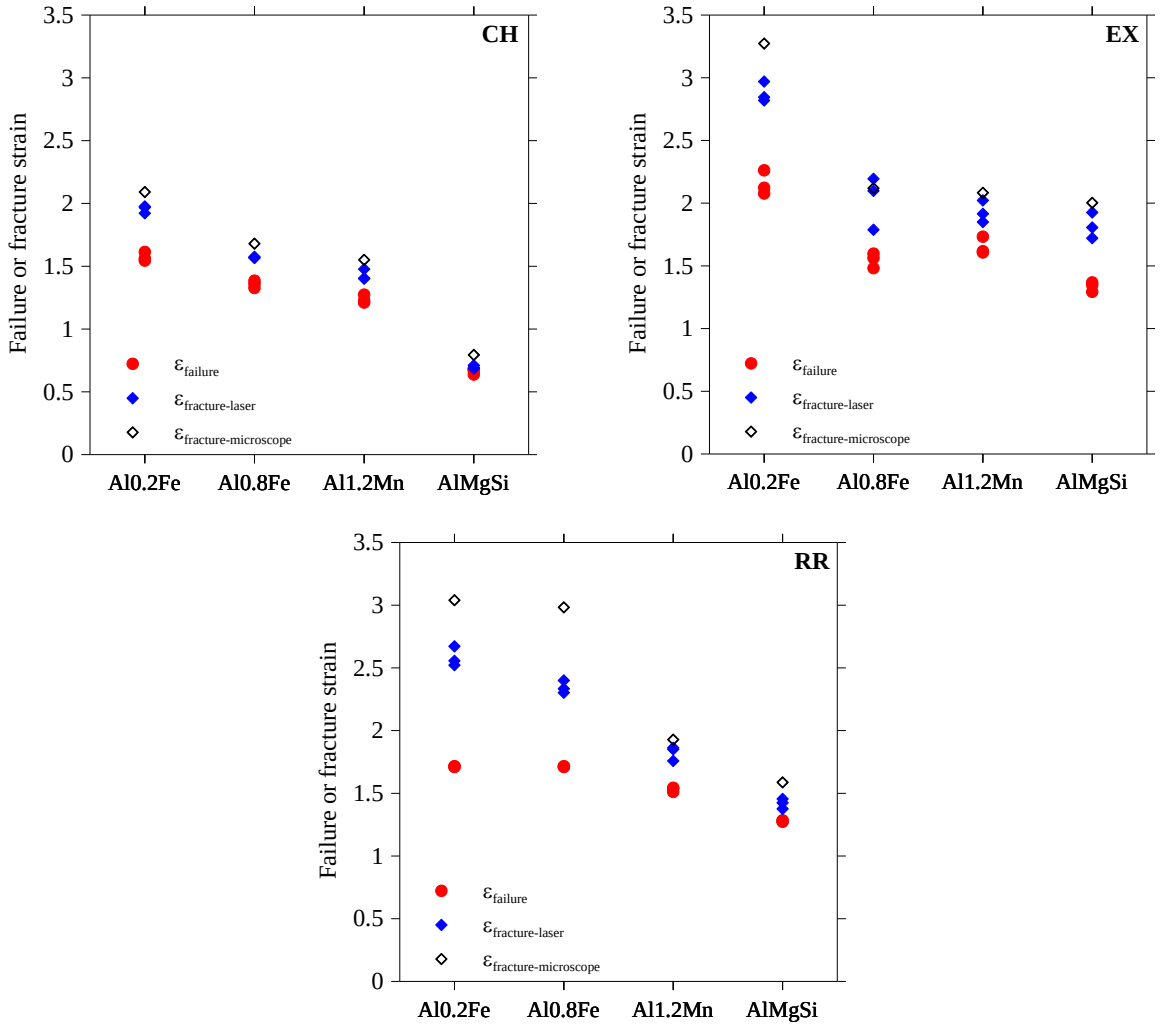

Figure 12. Comparison of failure and fracture strains from laser measurements with fracture strains from area measurements obtained with a microscope on the failed samples. All strains are logarithmic.